Stellar Birth Radii in the LMC: Insights into Chemodynamics, Radial Migration, and Star Formation across the Disk

Yuxi(Lucy) Lu; Bethany Garver; David L. Nidever; Joshua T. Povick; Nicolás Garavito-Camargo; Maria-Rosa L. Cioni; Danny Horta

The Astronomical Journal, 171:230 (11pp), 2026 April https://doi.org/10.3847/1538-3881/ae4a8d

Stellar Birth Radii in the LMC: Insights into Chemodynamics, Radial Migration, and Star Formation across the Disk

Yuxi(Lucy) Lu[1,2], Bethany Garver[3], David L. Nidever[3], Joshua T. Povick[3], Nicolás Garavito-Camargo[4,5], Maria-Rosa L. Cioni[6], and Danny Horta[7]

[1] Department of Astronomy, The Ohio State University, Columbus, 140 W 18th Avenue, OH 43210, USA
[2] Center for Cosmology and Astroparticle Physics (CCAPP), The Ohio State University, 191 W. Woodruff Avenue, Columbus, OH 43210, USA
[3] Montana State University, P.O. Box 173840, Bozeman, MT 59717-3840, USA
[4] Steward Observatory, University of Arizona, 933 North Cherry Avenue, Tucson, AZ 85721, USA
[5] Department of Astronomy, University of Maryland, College Park, MD 20742, USA
[6] Leibniz-Institut für Astrophysik Potsdam, An der Sternwarte 16, D-14482 Potsdam, Germany
[7] Institute for Astronomy, University of Edinburgh, Royal Observatory, Blackford Hill, Edinburgh, EH9 3HJ, UK
Received 2025 November 17; revised 2026 February 18; accepted 2026 February 23; published 2026 March 17

Abstract

The LMC and SMC are interacting dwarf galaxies offering a valuable testbed for studying galactic mergers. We investigate the LMC's chemodynamic history during its interaction with the SMC by inferring stellar birth radii using APOGEE DR17 data, first validated on a hydrodynamical simulation reproducing their interaction history. Using birth radii and stellar ages, we identify signatures of dynamical and chemical evolution across the LMC disk. The LMC's metallicity gradient steepened around 5, 3, and 1 Gyr ago, coinciding with enhanced star formation (SF). These events show distinct spatial patterns—initially inner-disk concentrated 5 Gyr ago, expanding outward by 3 Gyr, and becoming widespread with renewed central activity at 1 Gyr—likely reflecting changes in spin alignment if SF enhancements track the SMC's pericenter passages. After accounting for disk scale-length differences, inferred radial migration strength rises relative to Milky Way (MW) expectations at ages $<$5 Gyr and during major SF enhancements reported in the literature. The most -enriched stars formed 2–3 Gyr ago at birth radii of 2–4 kpc, the only epoch when SF was broadly distributed. Unlike the MW, the LMC lacks a clear [/M]-[Fe/H] bimodality, likely due to more centrally concentrated SF versus the MW's extended outer-disk SF. These results strongly constrain the LMC's assembly and its interaction with the SMC.

Unified Astronomy Thesaurus concepts: Large Magellanic Cloud (903); Chemical abundances (224); Galaxy evolution (594); Stellar dynamics (1596)

1. Introduction

Radial migration is the process by which stars undergo permanent changes in angular momentum due to dynamical interactions, often at corotation resonances of various galactic structures. These interactions can arise from transient spiral arms (e.g., J. A. Sellwood & J. J. Binney 2002; R. Roškar et al. 2008), overlapping resonances between the bar and spiral structure (e.g., I. Minchev & B. Famaey 2010), external perturbations (e.g., A. C. Quillen et al. 2009), or a slowing bar (e.g., H. Zhang et al. 2025). Stars moving away from their birth locations means one cannot and should not equate an age-resolved evolution of a galaxy with its temporal evolution (e.g., I. Minchev et al. 2013; N. Frankel et al. 2019; S. Sharma et al. 2022; Y. L. Lu et al. 2022b; B. Ratcliffe et al. 2023). One such common misconception is using "look-back time" and "age" interchangeably. Metallicity and detailed elemental abundance gradients measured at a given stellar age are typically shallower and exhibit larger scatter about the underlying linear relation than gradients evaluated at the same look-back time because stars observed at a given age that formed at that look-back time have subsequently had time to migrate across the galaxy. They also typically move outward as a population (flattening the gradient) due to the exponential surface density profile in galaxies (e.g., I. Minchev et al. 2013). Although individual stars have comparable probabilities of migrating inward or outward near the corotation resonance, the higher stellar density at smaller radii results in a net outward redistribution when averaged over the population. As a result, in order to infer the true formation history of a galaxy, it is important to take into account the effects of radial migration.

Extensive efforts have been devoted to identifying the effects and signatures of radial migration in the Milky Way (MW). For example, studies have focused on understanding the metallicity distribution functions and the age–metallicity relation (e.g., J. A. Sellwood & J. J. Binney 2002; S. R. Loebman et al. 2016; Y. L. Lu et al. 2022b; J. Lian et al. 2022), the formation of the high- and low- disks (e.g., S. Sharma et al. 2022; C. L. Sahlholdt et al. 2022; Y. L. Lu et al. 2024b), the temporal evolution of the metallicity gradient (e.g., I. Minchev et al. 2018; B. Ratcliffe et al. 2023; Y. L. Lu et al. 2024b), and many more (e.g., N. Frankel et al. 2020). Despite extensive efforts in the MW, the effects of radial migration in external galaxies have received comparatively little attention. Recently, studies have shown that inferring the spatially resolved star formation history (SFH) for disk galaxies without taking into account radial migration can introduce large uncertainties (J. P. Bernaldez et al. 2025; I. Minchev et al. 2026; B. Ratcliffe et al. 2026).

To begin addressing this gap, we start with the closest galaxy pairs to us—the Magellanic Clouds (MCs) system. The

LMC and the SMC have photometric observations for individual stars down to the main sequence (e.g., the VISTA Survey of the Magellanic Clouds, SMASH; N. J. G. Cross et al. 2012; M. R. L. Cioni 2016; D. L. Nidever et al. 2017, 2021), providing us with a detailed SFH of the MCs (S. Rubele et al. 2018; T. Ruiz-Lara et al. 2020; A. Mazzi et al. 2021; P. Massana et al. 2022; S. Saroon et al. 2025). Moreover, detailed abundances are also available (D. L. Nidever et al. 2020) for a subset of the upper red giant branch (RGB) stars through the APOGEE–2S (J. C. Wilson et al. 2019). These observations of individual stars provide us with the exact dataset we need to obtain birth radii (R_b, the galactic-centric radius of where the stars are born). Combining age, R_b, element abundances, and the SFH, we can begin to uncover the true chemodynamic history of the LMC and assess the role of major mergers in shaping galaxy evolution.

In this paper, we test the method described in Y. L. Lu et al. (2024b) on a hydrodynamical simulation of the LMC (B. Garver et al. 2026, in preparation) that is set up to reproduce the formation and interaction history of the LMC and SMC. The description of the simulation is in Section 2.1. After successfully inferring R_b from the simulation (Section 2.3), we apply this method to the LMC observations (Section 2.2) to infer R_b and the temporal evolution of the metallicity gradient (Section 2.4). In Section 3, we look at the radial migration strength, preferred star formation (SF) radii across time, and the chemodynamic history of the LMC in [/M]-[Fe/H] space. Finally, in Section 4, we discuss how insights from the LMC–SMC merger inform our understanding of the two-infall model for the MW.

2. Data and Methods

2.1. Simulation Data

The orbit of the MCs is taken from the B. Garver et al. (2026, in preparation) suite of 8000 N-body interaction simulations. This produces closer encounters 2 Gyr and 150 Myr ago. We use the smooth particle hydrodynamics+N-body tree-code GASOLINE (J. W. Wadsley et al. 2004, 2017) to simulate the MCs and MW. The LMC and SMC are simulated in isolation for 6 Gyr and are then combined with the MW and evolved for another 2.5 Gyr. The simulated LMC begins with a gas disk of mass $7.18 \times 10^9 M_\odot$ and a dark matter halo of mass $1.81 \times 10^{11} M_\odot$. It is evolved in isolation for 6 Gyr during which time some of the gas forms into stars. Then it is combined with an SMC and MW model, and the combined simulation is evolved for a further 2.5 Gyr. GASOLINE tracks the [Fe/H] and [O/Fe] of the star and gas particles, as well as the birth times and locations of the stars. The simulation uses 20% feedback, which means that 20% of the 10^{51} erg of energy from supernovae is injected as thermal energy into the interstellar medium.

2.2. Observational Data

The 6000 LMC RGB stars are taken from APOGEE (S. R. Majewski et al. 2017) and the abundances from APOGEE DR17 (Abdurro'uf et al. 2022), with spectra reduced with the APOGEE reduction pipeline (D. L. Nidever et al. 2015). Stellar ages were derived following the method in J. T. Povick et al. (2024) using observed APOGEE spectroscopic parameters (Teff, $\log g$, [Fe/H], and [/Fe]) and multiband photometry from Gaia (Gaia Collaboration et al. 2016, 2021a) and the Two Micron All Sky Survey (M. F. Skrutskie et al. 2006) with PARSEC isochrones (L. Girardi et al. 2002; A. Bressan et al. 2012; P. Marigo et al. 2017). Distances for the stars were found using the red clump model from SMASH (Y. Choi et al. 2018a, 2018b) and assuming that the RGB stars lie close to the disk plane. For each star, model photometry and $\log g$ were interpolated from the isochrones as functions of Teff, [Fe/H], [/Fe], and a trial age. Since the isochrones are based on scaled-solar models, the [Fe/H] are adjusted with the measured [/Fe] following M. Salaris et al. (1993) with updated coefficients from J. T. Povick et al. (2024). The trial age was then adjusted until the model photometry and $\log g$ best matched the observed values. Validation with the APOKASC asteroseismic sample (with accurate masses and ages) indicates that the age uncertainties are 20% (see Figure 16 in J. T. Povick et al. 2024). The selection function assigns each star a representative "stellar mass," referring to the total mass in stars at a given location. The selection correction procedure accounts for both the observational brightness limits and the contribution of unobserved stars using synthetic photometry from isochrones. Details of the method are described in Section 9 in J. T. Povick et al. (2024).

2.3. Recovering Birth Radii for LMC Simulation

It is known that the LMC is highly perturbed dynamically by the interaction with the SMC and MW. As a result, it is important to test whether inferring birth radii for such a galaxy is feasible. In Y. Lu et al. (2024a), we explored the possibility of obtaining R_b for external galaxies using the method described in Y. L. Lu et al. (2024b), which is a method improved upon I. Minchev et al. (2018), using a set of updated assumptions (Y. Lu et al. 2022a). Using the Numerical Investigation of a Hundred Astronomical Objects (NIHAO; L. Wang et al. 2015) cosmological simulations, we determined it is important to consider the effects of radial migration in an LMC-mass galaxy when understanding its formation history. Given the LMC's halo mass ($18.8^{+3.5}_{-4.0} \times 10^{10} M_\odot$; N. Shipp et al. 2021) and the estimated LMC's diskiness $\langle v_\phi /\sigma_v$ 2.8 (Figure B.5. in Gaia Collaboration et al. 2021b), we also determined birth radii can be inferred with 25% uncertainty in the LMC. In addition, we tested our method on a LMC-mass dwarf galaxy in NIHAO, `1.64e11`, where a similar LMC/SMC mass-ratio interaction happened within the last 2 Gyr, and were able to recover birth radii for this galaxy. In this paper, we further test the possibility of inferring birth radii and dynamical properties, such as the radial migration strength, using the simulation described in Section 2.1, which is intended to reproduce the orbital history of the LMC, SMC, and the MW.

Since R_b inference can only be applied to stars formed in the galactic disk, we selected stars in the simulation that are born within 15 kpc of the galactic center with birth vertical height, $|z_{\rm bir}| < 1$ kpc. Changing to select $|z_{\rm bir}| < 0.5$ kpc does not alter our result significantly. We then scale the metallicity so that the standard deviation and median match those of the observations (median: −0.77 dex, std: 0.23 dex). To mimic the observational uncertainty, we perturbed the metallicity and age in the simulation by their typical observational uncertainty (0.015 dex for metallicity and 20% for age).

To infer R_b, we first applied the procedure described in Y. L. Lu et al. (2024b) to measure the range in metallicity in

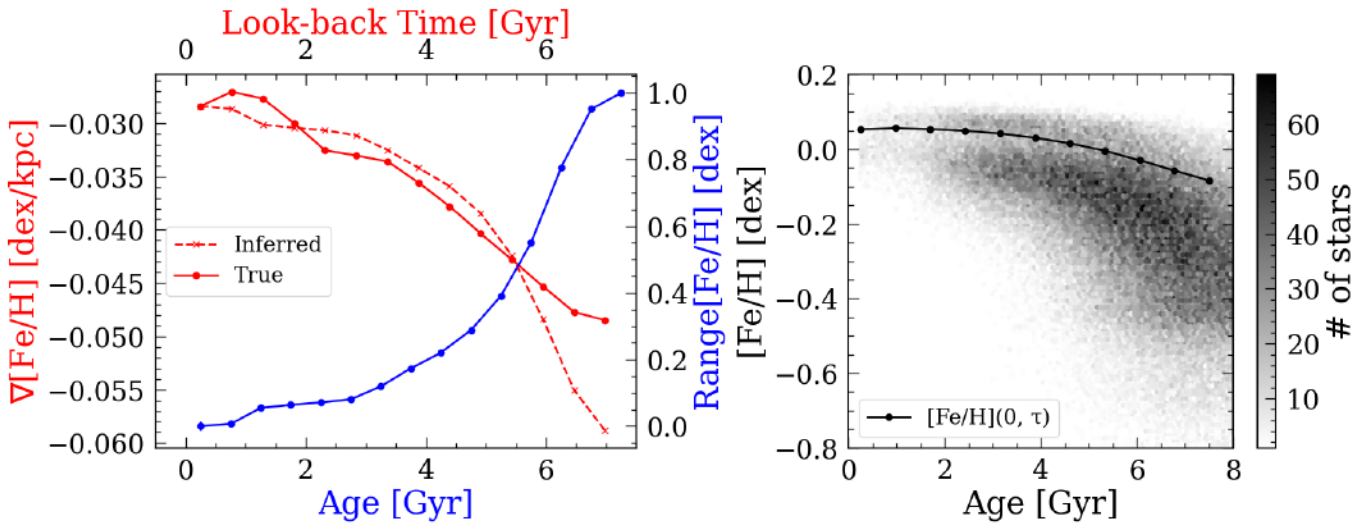

Figure 1. Key plots for inferring the metallicity evolution of the simulated LMC galaxy. Left: the blue line shows the range of metallicity, Range[Fe/H], as a function of age, using a bin width of 0.5 Gyr. The range is measured using the difference between the 95th-percentile and the 10th-percentile of [Fe/H] in mono-age populations to account for more stars in the inner galaxy compared to the outer. The red solid line shows the true metallicity gradient, [Fe/H], as a function of look-back time, measured using the true R_b and [Fe/H] in each mono-age population. The red dashed line is the inferred metallicity gradient using Equation (1). We can reproduce some of the key features, such as the steepening, in the metallicity gradient, and the median absolute deviation from the true metallicity gradient is 6% or 0.002 dex kpc^{-1}. Right: the evolution of metallicity at the galactic center is shown in the black solid line. The background shows the histogram of the age–metallicity relation for this simulated galaxy. Again, the most metal-enriched stars at every age bin should represent the metallicity of the LMC center at that look-back time, assuming a negative metallicity gradient is present at all ages after the disk has started to form.

mono-age populations. The method stated that the metallicity gradient as a function of look-back time can be directly inferred using the range in metallicity as a function of age with a linear relation. Since fewer stars are formed in the outer disk, which should be the most metal poor if we assume a negative metallicity gradient due to inside-out formation, we selected 10th-percentile for the lower limit instead of 5th-percentile when calculating the range of metallicity (Range[Fe/H]). We inferred the metallicity gradient ([Fe/H]) as a function of look-back time (τ) using Equation (1) in Y. L. Lu et al. (2024b):

$$\nabla[\mathrm{Fe/H}](\tau) = a \quad \mathrm{Range[Fe/H](age)} + \nabla[\mathrm{Fe/H}](0), \quad (1)$$

where [Fe/H](0) $= -0.028$ dex kpc^{-1} is the metallicity gradient at redshift 0, inferred using the youngest stars, and a is the scaling factor, of which we used -0.031 kpc^{-1} to ensure the birth radii distribution is sensible, where the youngest stars (<1 Gyr) have not migrated much (<1 kpc) and the oldest stars are mostly formed >0 kpc (See Figure 4 in Y. L. Lu et al. 2024b). The scaling factor, the range, the inferred gradient evolution, and the true gradient evolution for the simulation are shown in the left plot of Figure 1. For better understanding, the range in metallicity (Range[Fe/H]) provides the shape of the inferred metallicity gradient, the current-day metallicity gradient, [Fe/H](0), provides the anchor point, and the scaling factor, a, constrains the range, or the steepest point, for the metallicity gradient.

Birth radii are then inferred with age and metallicity measurements using Equation (3) in Y. L. Lu et al. (2024b):

$$\mathrm{R_b(age,\ [Fe/H])} = \frac{\mathrm{[Fe/H]} - \mathrm{[Fe/H]}(0,\ \tau)}{\nabla\mathrm{[Fe/H]}(\tau)}, \quad (2)$$

where [Fe/H](0, τ) is inferred by first taking the 95th-percentile of the metallicity in mono-age populations (as shown in the right plot of Figure 1). This is because, assuming the metallicity gradient is always negative, the metallicity of the center of the galaxy at a given look-back time will always contain the most metal-enriched stars of the same age. We then shift [Fe/H](0, τ) so that stars <1 Gyr have $R - R_b$ peaks close to 0, as these young stars should not have much time to migrate. The shifted value is determined to be -0.04 dex.

Figure 2 shows the inferred birth radii using the method described in this section compared to the truth for the simulation. We are able to infer birth radii with a root mean square error (RMSE) of 1.5 kpc and a bias of -0.4 kpc for stars <6 Gyr. The bias could affect the absolute values of our results, but since the birth radii in this paper are primarily used to rank the locations where stars are born, the impact should be small as long as the ranking is preserved, i.e., stars formed in the outer disk have larger inferred R_b compared to those formed in the inner galaxy, and the bias should not significantly affect our conclusions regarding star-forming regions as a function of look-back time or the inferred migration strength.

Figure 3 shows the [Fe/H]-R_b distribution (background density plot), the true gradient (red, solid lines), and the inferred gradient (red, dashed lines) for three different look-back time bins. To infer birth radii, we assume all stars follow a perfect relation shown as the dashed line. The fits do not perform well for stars in the outer galaxy, as the gradient is not exactly linear, and most stars are born in the inner galaxy. This could explain the bias seen for stars in the outer disk (Figure 2). One other source of uncertainty comes from the fact that there is scatter around the relation. For stars >6 Gyr, the stellar disk is still settling from the initial condition, and since this method can only be applied to stars after the stellar disk has mostly formed (Y. Lu et al. 2022a), it is not surprising we are not able to reproduce the true metallicity gradient while

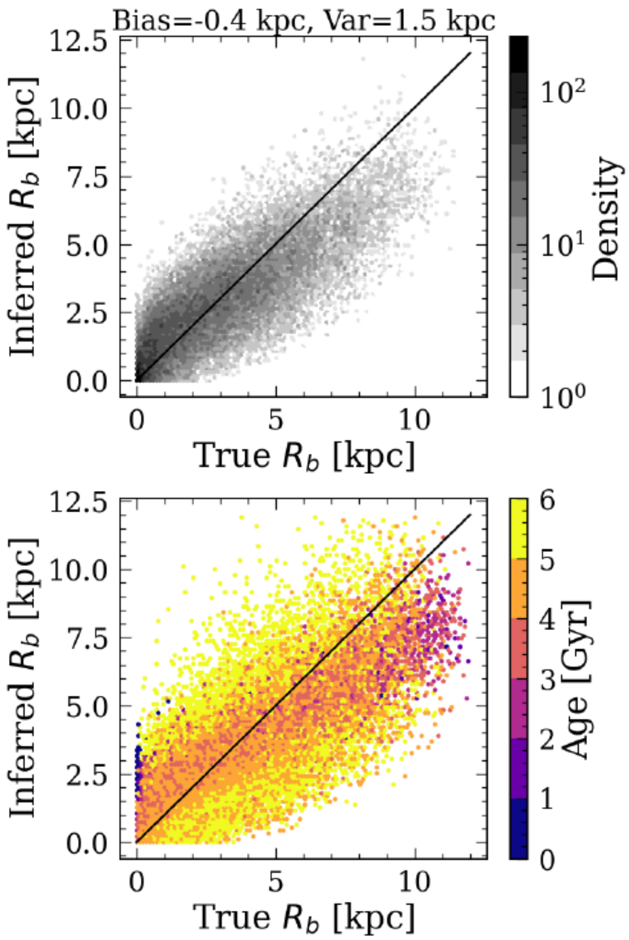

Figure 2. Histogram of the true birth radii from the simulated LMC versus the inferred birth radii using the method described in Section 2.3, colored by the number of stars (top) and the median age (bottom). We are able to successfully infer birth radii with a bias of −0.6 kpc and a RMSE of 1.5 kpc for stars <6 Gyr.

the disk is still settling and the scatter around the metallicity gradient is larger (see Figure 3, right panel).

Finally, Figure 4 compares the R_b distribution as a function of age and the radial migration strength in the simulation for stars <6 Gyr. The left panel presents the median and 1.5∗ Median Absolute Deviation (MAD) of R_b in each age bin using the truth R_b ($R_{b,\mathrm{truth}}$; blue) and the inferred R_b ($R_{b,\mathrm{inf.}}$; black). Ages include a 20% uncertainty convolved to mimic observation data. The overall shape of the median and dispersion is reproduced down to 1 Gyr. This is not surprising as we are only able to infer birth radii to the accuracy of 1.5 kpc, and most stars <1 Gyr in the simulation are born within the central 1 kpc. The right panel shows the radial migration strength (σ_{RM}); the true migration strength, shown as blue points, is calculated with $1.5 * \mathrm{MAD}(R - R_{b,\mathrm{true}})$, where R and $R_{b,\mathrm{true}}$ are the current and true R_b, respectively. The inferred migration strength, shown as black crosses, is calculated with $\sigma_{\mathrm{RM,inf.}} = \sqrt{(k * \mathrm{MAD}(R - R_{b,\mathrm{infer}}))^2 - (\sigma_{\mathrm{unc.}})^2}$ to account for the uncertainty in inferring R_b, where $R_{b,\mathrm{infer}}$ is the inferred R_b, $\sigma_{\mathrm{unc.}}$ is the uncertainty in which we can infer R_b, and $k = 1.5$ is the factor to convert from MAD to standard deviation. When the total scatter, $k * \mathrm{MAD}(R - R_{b,\mathrm{infer}}) < 1.5$ kpc, the quantity inside the square root becomes negative and therefore nonphysical. In these cases, we set $\sigma_{\mathrm{RM,inf.}} = 0$ when this happens. Uncertainties in radial migration strength from the inferred R_b are obtained via bootstrapping, perturbing R_b within 1.5 kpc (the variance from Figure 2) and age within 20% (the typical observational age uncertainty).

2.4. Recovering Birth Radii for the LMC

Before applying the method to the observational data, we correct for the selection function by first identifying the star with the smallest represented stellar mass. Each remaining star is then replicated according to the number of such minimum-mass stars it represents in the sample. For each replicated instance, we perturb the stellar age and chemical abundances within their quoted uncertainties before including it in the analysis.

After accounting for the selection function, we apply the method described in the previous section to the data, using age bins between 0 and 8 Gyr, with a width of 0.5 Gyr to obtain Range[Fe/H]. To calculate the uncertainty, for each age bin, we performed bootstrapping 100 times by randomly selecting 200 stars each time and recomputed the percentiles. For reference, we have over 800 stars in each age bin, and changing the number of stars we select to be 100 or 400 does not impact our result. The uncertainty is then taken to be the standard deviation of all the calculations. The left panel of Figure 5 shows the measured Range[Fe/H] as a function of age (top axis). The center metallicity evolution is determined using the 80th-percentile of the metallicity in mono-age bins, as we did for the simulation. The result is shown as the black solid line in the right panel of Figure 5.

We inferred the birth metallicity gradient as a function of look-back time using Equation (1), where $a = -0.2\ \mathrm{kpc}^{-1}$ and $[\mathrm{Fe/H}](0) = (-0.2\ \mathrm{Range[Fe/H]}(0) - 0.022)$ dex/kpc, where −0.022 is the current-day metallicity gradient and Range[Fe/H](0) = 0.29 dex is the current-day Range[Fe/H], both measured using stars <0.7 Gyr. This ensures Equation (1) can reproduce the current-day gradient with the current-day Range[Fe/H]. We determine the value of a so that the birth radii distribution is sensible, where stars born today have not migrated much, meaning the $R - R_b$ distribution peaks close to 0 and the width of the Gaussian is <2 kpc for the youngest stars (<1 Gyr; see Figure 6); the oldest stars are mostly formed >0 kpc; and the birth metallicity gradient at a look-back time is at least as steep as the observed metallicity gradient for stars of the same age, since the observed gradient is always shallower than the birth gradient—a natural phenomenon in galaxies with decreasing surface density toward the disk outskirt. The uncertainty on the inferred birth metallicity gradient is determined by bootstrapping the slope 100 times with Range[Fe/H] measurements perturbed within their uncertainty. We mark the times (0.5, 1.1, 2, 3, and 5 Gyr) where SF is enhanced in the LMC (P. Massana et al. 2022), in which the enhancements of 0.5, 1.1, 2, and 3 Gyr are thought to be caused by the interaction between the MCs, as similar peaks are also found in the SMC. It is unclear what causes the enhancement at 5 Gyr, as this is only seen in the LMC but not in the SMC. However, S. Saroon et al. (2025) finds enhancement in the SMC around the same time in the outskirts of the galaxy.

Steepening in the metallicity gradient is observed at 1 and 5 Gyr. This is also seen in the MW (e.g., Y. L. Lu et al. 2024b) and MW-like simulations (e.g., T. Buck et al. 2023; B. Ratcliffe et al. 2024). They are typically caused by the sudden increase in

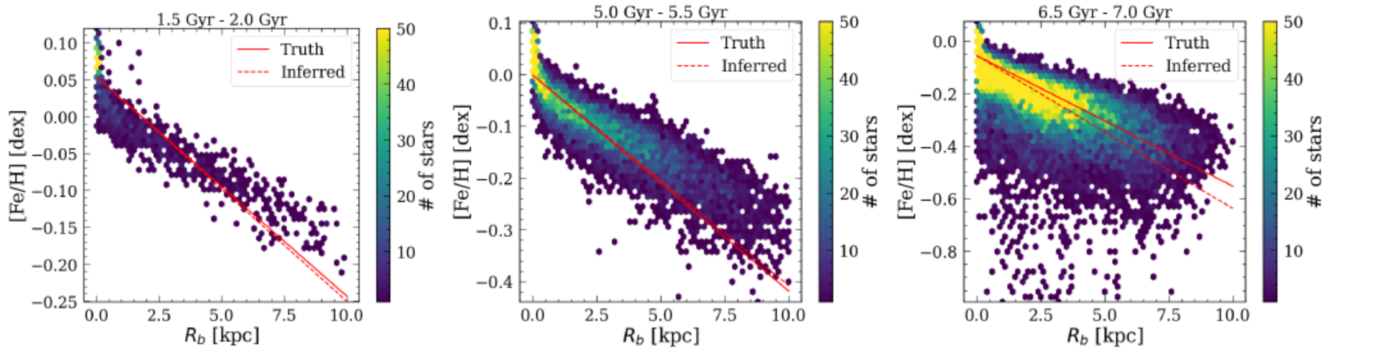

Figure 3. Metallicity–R_b relation for stars in the LMC simulation during interaction phase between the LMC and SMC (1.5–2 Gyr; left), isolation phase (5–5.5 Gyr; middle), and settling phase (6.5–7 Gyr; right). The solid lines show the true metallicity gradient, and the dashed line shows the inference from Range[Fe/H]. The linear relation does fit the outer galaxy well, as the Metallicity–R_b relations are not exactly linear, especially in the inner galaxy. This causes the bias for inferring R_b for the outer galaxy (see Figure 2).

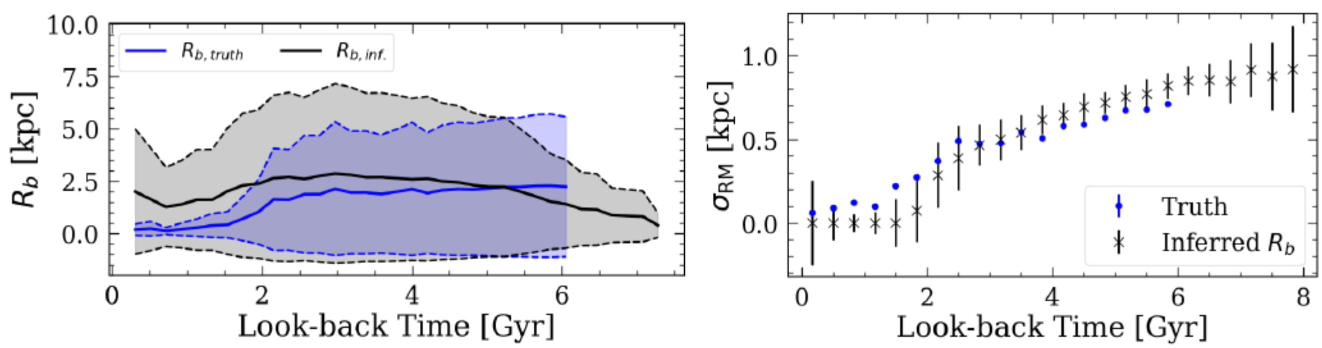

Figure 4. Left: the median and the 1.5∗MAD of the birth radii distribution as a function of age using the true R_b ($R_{b,\rm truth}$) and age shown in blue, and the inferred R_b ($R_{b,\rm inf.}$) and true age convolved with a 20% uncertainty in black. Right: the true migration strength (blue points) compared to the migration strength measured using inferred R_b (black crosses with error bars) for the simulation. The uncertainty in the inferred R_b of 1.5 kpc (see Figure 2) is accounted for by subtracting it in quadrature from the total scatter. When the total scatter is <1.5 kpc, we set the radial migration strength to be 0, as the quantity inside the square root becomes negative and therefore nonphysical. The uncertainties are measured with bootstrapping R_b with a width of 1.5 kpc and age with a width of 20% of its value. Both relations using inferred R_b extend beyond 6 Gyr due to the imposed age uncertainty. We are able to reproduce the general shape for both the R_b distributions and the radial migration strength.

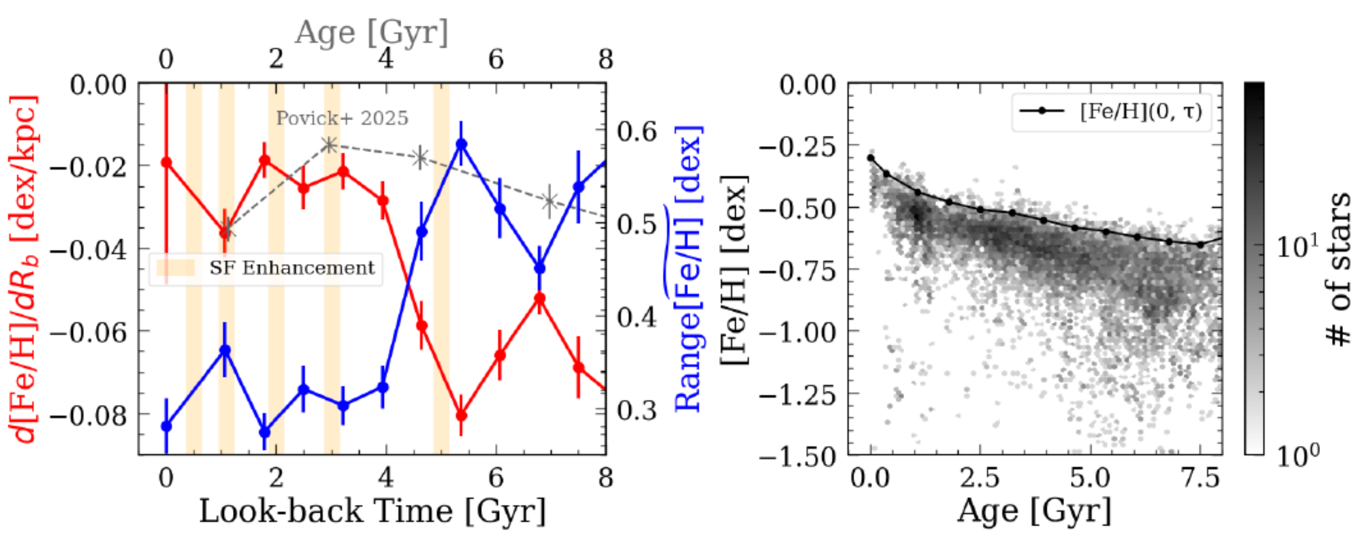

Figure 5. Similar to Figure 1 but with the LMC observational data. The red solid line shows the inferred metallicity gradient as a function of look-back time, derived using the range in metallicity. The orange shaded areas are enhancements in SF at 0.5, 1.1, 2, 3, and 5 Gyr (P. Massana et al. 2022). The gray dashed line shows the metallicity gradient as a function of age taken from J. T. Povick et al. (2025). The observed metallicity gradient as a function of age is shallower than the inferred metallicity gradient at birth due to radial migration. Steepening in the metallicity gradient, defined as where the local minima are, is observed at or close to the times of increased SF around 1 and 5 Gyr. This is also seen in the MW (e.g., Y. L. Lu et al. 2024b) and MW-like simulations (e.g., T. Buck et al. 2023; B. Ratcliffe et al. 2024).

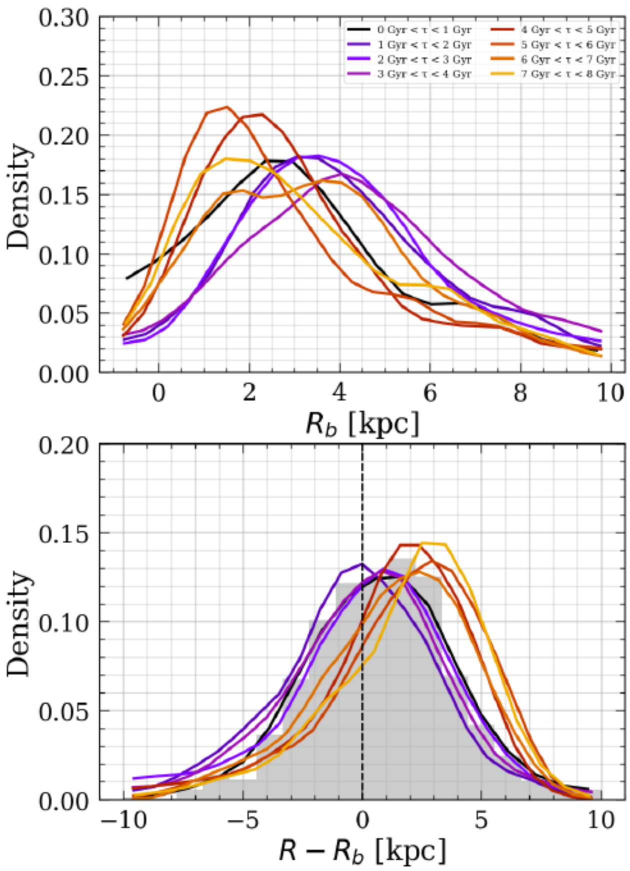

Figure 6. Normalized histograms showing the distribution of birth radii (top) and the amount of migration (bottom) for stars of different ages (as indicated in the legend). For each histogram, we selected the number of bins to be the integer part of $\sqrt{N}/2$, where N is the number of stars in each age bin. We then plotted the smoothed histograms using a 1D Gaussian kernel with a width of 1 kpc for better visualization. The gray histogram in the bottom panel shows the unsmoothed distribution for stars younger than 1 Gyr. We expect the migration distribution of these youngest stars to peak near 0 kpc with a characteristic width of <2 kpc, reflecting their limited movement since birth.

the cold gas disk size from lower metallicity gas accreted from infalling satellites. As a result, even if the SMC did not show enhancement in SF in its main body, the signature at 5 Gyr still matches with those of a gas accretion event.

Finally, we estimated the birth radii of stars in the LMC using Equation (2). For each star, we performed 50 Monte Carlo realizations of the birth radius calculation, drawing age, [Fe/H], and [Fe/H](τ) from Gaussian distributions centered on their measured values and with standard deviations equal to their respective uncertainties. The final birth radius and its uncertainty were taken as the median and half of the difference between the 84th-percentile and the 16th-percentile of these 50 realizations. Figure 6 presents the resulting birth radius and migration distributions for stars grouped by age. As expected from inside-out galaxy formation, older stars should originate in the inner disk relative to younger stars. Additionally, the youngest stars, which have not had much time to migrate, exhibit a median radial migration close to 0 kpc, with a characteristic dispersion (migration strength) of approximately 1.5 kpc.

It is worth pointing out that C. Gallart et al. (2009), and recently, N. Frankel et al. (2025), suggested that the LMC could form outside-in based on the scale length in mono-[Fe/H], mono-age populations. We could not test this in this work, as overall inside-out formation is one of our assumptions. However, according to individual R_b distributions, the youngest stars are formed more in the inner disk, and some of the oldest stars (>6 Gyr) are formed in the outer disk. We will revisit this topic in Section 3.2.

3. Results

3.1. Where and When the LMC Stars Are Formed

With birth radii, we can now picture a more detailed SF history—not only when stars are formed but also where. Figure 7 shows R_b as a function of look-back time, while the black vertical lines show the center of enhancement of SF episodes indicated in P. Massana et al. (2022) or A. Mazzi et al. (2021), the red vertical lines show the model predictions of the pericenter passages of the SMC to the LMC from model 2 in G. Besla et al. (2012), and the text on top shows the possible first pericenter passage of the LMC with the MW predicted in E. Vasiliev (2024). The blue solid line and the blue dashed lines show the median and 1.5∗MAD of R_b. Combining information shown for the birth metallicity gradient in Figure 5, we can conclude that >6 Gyr, the LMC forms inside-out, with most of the stars forming with galactic radius <2 kpc at 8 Gyr to <6 kpc at 6 Gyr.

During the first enhancement of SF at 5 Gyr according to P. Massana et al. (2022), most stars are born in the inner disk while the metallicity gradient steepens and the center metallicity slightly increases. Enhancement of SF in the central kpc and suppression of SF in the outer disk could happen during a passage where the primary and secondary galaxies have aligned disk spin orientations, and gas from the secondary quickly funnels in the center of the primary (e.g., J. Moreno et al. 2015). If this is caused by the passage of the SMC, similar enhancement should be seen in the SMC. This is seen in S. Rubele et al. (2018) but is not in P. Massana et al. (2022), possibly because of the difference in spatial selection. After this starburst, the LMC gradient then quickly flattens between 4 and 5 Gyr. During the SF enhancement at 3 Gyr, most stars are formed in the center or outer disk, between 2 and 6 kpc. The metallicity gradient also decreases, showing obvious expectations from gas-rich merging satellite (e.g., P. Torrey et al. 2012; T. Buck et al. 2023; Y. L. Lu et al. 2024b). If this is triggered by the pericenter passage of the SMC, the disk spin orientations between the MCs are likely not aligned or perpendicular. The enhancement at 1.1 Gyr shows even a stronger steepening of the metallicity gradient, with stars forming across the LMC and a significant enhancement in SF in the center, between 1 and 4 kpc, suggesting aligned disk spin orientations. Finally, the enhancements identified by P. Massana et al. (2022) at 0.5 and 2 Gyr show no significant imprints in our R_b distribution. This suggests the SMC and LMC close encounters likely happened around the enhancement in SF 1, 3, and perhaps 5 Gyr, agreeing with predictions from some simulations (e.g., G. Besla et al. 2012; S. A. Pardy et al. 2018). The SF region also suggested a change in disk alignments between the MCs during the multiple passages.

However, if the SF enhancements do not track the pericenter passages of the SMC but instead the model 2 predictions from G. Besla et al. (2012) are the true passage times, the SMC/LMC disks are likely antialigned across all passages.

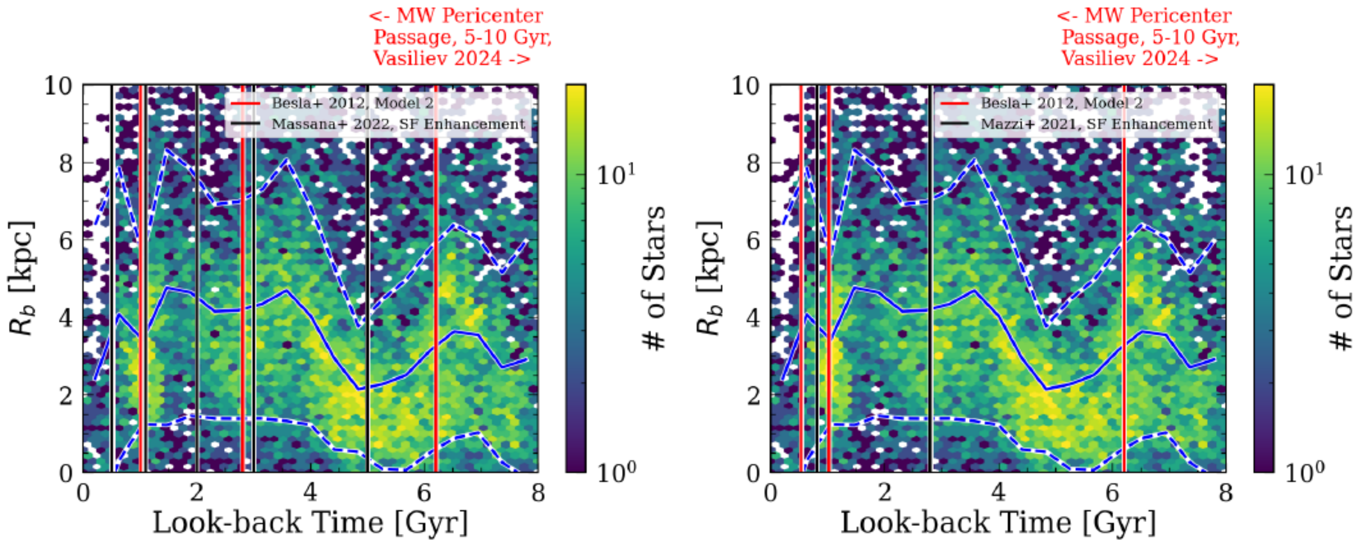

Figure 7. The detailed SFH of the LMC compared with SF enhancements from P. Massana et al. (2022) and A. Mazzi et al. (2021). The blue solid line shows the median star-forming R_b, and the dashed lines show 1.5∗MAD. The black lines are the center of the SF episodes identified from the literature as indicated in the legends, the SMC pericenter passage times are taken from model 2 predictions in G. Besla et al. (2012), and the possible first passage time with the MW 5–10 Gyr ago is shown on the top (E. Vasiliev 2024). The steepening in the metallicity gradient and the increase in SF around 1.1, 3, and perhaps 5 Gyr match our expectations for an infalling satellite with varying disk alignments. In this case, it is likely the SMC or the LMC passage with the MW. The location of the starbursts suggests aligned disk spin orientations between the merging galaxies during the 5 and 1.1 Gyr passages and misaligned or perpendicular disk spin orientations for the 3 Gyr passage based on results from simulation analysis (J. Moreno et al. 2015). The enhancements at 0.5 and 2 Gyr taken from P. Massana et al. (2022) have no significant signatures in our R_b distribution. It is also interesting to point out that the SF happens at the outer disk for the three pericenter predictions, suggesting the alignments between the LMC and SMC disks do not change if the predictions from the model are correct.

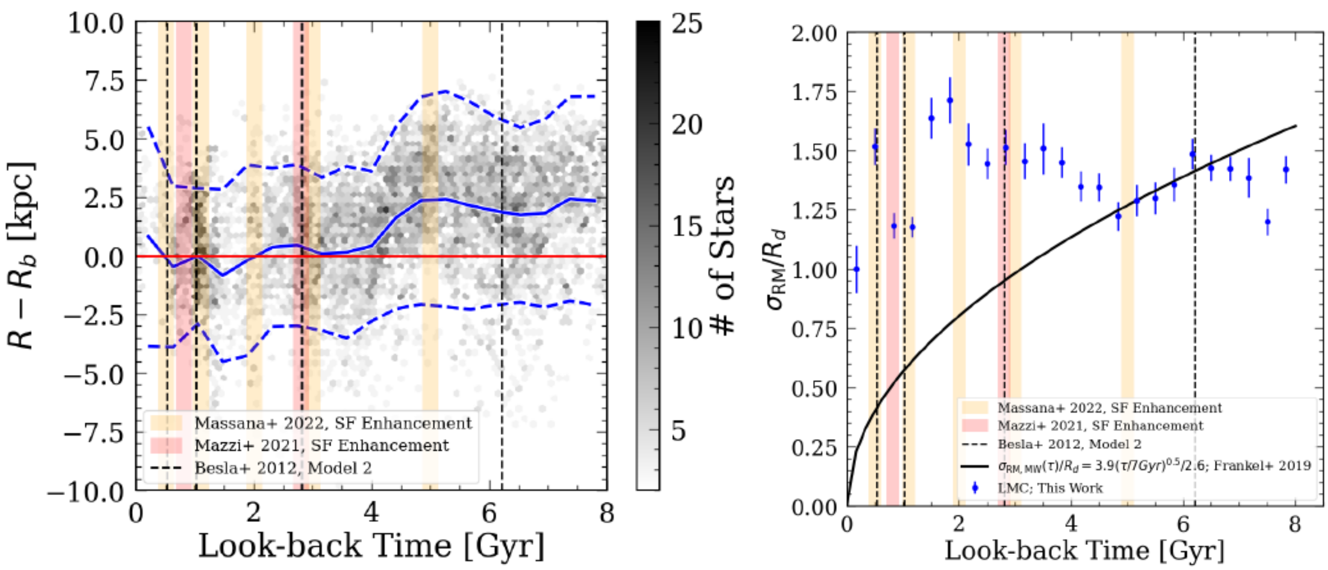

Figure 8. Left: $R - R_b$ for the LMC stars, where the blue solid line shows the median and the blue dashed line shows the 1.5∗MAD. The orange and red vertical lines show the SF enhancements taken from P. Massana et al. (2022) and A. Mazzi et al. (2021), respectively. The black dashed lines show the model prediction from G. Besla et al. (2012). Right: radial migration strength as a function of look-back time for the LMC data (blue points). In order to infer the migration strength, we subtracted 1.5 kpc in quadrature from the total scatter to account for the measurement uncertainty in the R_b inference. The inferred migration strength was then scaled by the LMC scale length (1.47 kpc; D. R. Alves 2004). The black line shows the analytic solution of the radial migration strength for the MW, taken from N. Frankel et al. (2019), also scaled with the MW scale length of 2.6 kpc (J. Bland-Hawthorn & O. Gerhard 2016). The LMC stars show an increase in migration strength at 5 Gyr compared to the MW could be caused by a higher uncertainty in the observation compared to the simulation (>1.5 kpc) for this age range or a physically larger strength caused by interactions with the SMC and the MW.

This can be inferred as during all three of these pericenter passages predicted from the model, most stars are formed in the middle or outer disk, suggesting the star-forming gas did not funnel in the inner LMC, and the disks are likely antialigned (J. Moreno et al. 2015). The size of the star-forming region (indicated by the blue dashed lines) also increased close to the times when the SMC was predicted to be at the pericenter passages with the LMC according to model 2.

3.2. Radial Migration Strength in the LMC

We quantify the radial migration strength by looking at the median and width of the $R - R_b$ distributions as a function of

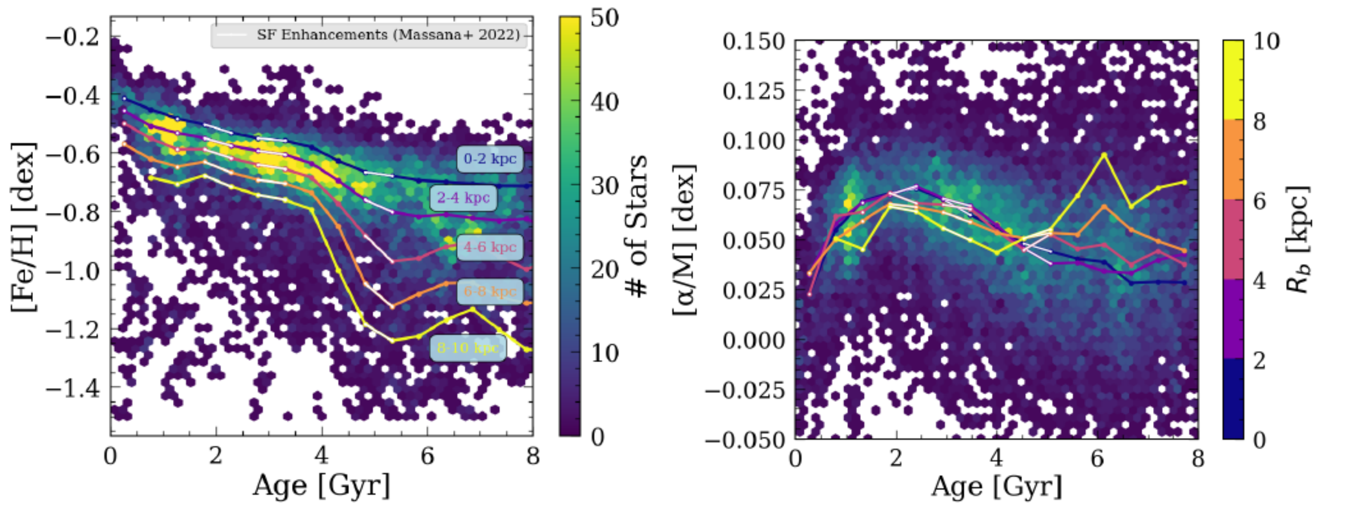

Figure 9. The age–metallicity (left) and the age–[/M] relations are plotted as density in the background, and the colored lines show the median temporal evolution in each mono-R_b population. The points on each line are separated equally in age with a difference of 0.5 Gyr. These tracks place additional constraints on the gas accretion and SFH at various locations and times. For example, combining with the SF region shown in Figure 7, at 5 Gyr, the LMC accreted a large amount of pristine gas at all radii (drop in [Fe/H] in all radii in the left panel) that increased the SFE in the inner disk (from Figure 7). This led to a decrease in [/M] in the outer disk since there was no SF and an increase of [/M] in the inner disk where most stars were formed, contributing to the element reservoir via SN II.

look-back time, where the median represents the overall migration of a mono-age population and the width quantifies the strength. Figure 8 shows the radial migration for the LMC stars as a function of look-back time, where the left plot shows the full distribution with median (blue solid line) and 1.5∗MAD (blue dashed line), and the right plot shows the standard deviation ($\sigma_{\rm RM}$) as a function of look-back time for the LMC data (blue points). The migration strength is measured to be 1.5∗MAD($R - R_b$) to account for outliers, and 1.5 kpc is subtracted in quadrature to account for the intrinsic measurement uncertainty, assuming the observation exhibit a similar uncertainty as the simulation (see Figure 2). For comparison, we also plotted the analytic model for the MW taken from N. Frankel et al. (2019). The orange and red lines are the SF enhancements taken from P. Massana et al. (2022) and A. Mazzi et al. (2021), respectively. The predictions for the pericenter passages taken from G. Besla et al. (2012) model 2 are plotted as dashed vertical lines. We scaled the strength by the scale length, R_d (2.6 for the MW and 1.47 for the LMC; D. R. Alves 2004; J. Bland-Hawthorn & O. Gerhard 2016). After scaling by scale length, radial migration strength in all galaxies should be similar (e.g., Y. Lu et al. 2024a). The LMC has a slightly higher migration strength $<$ 5 Gyr, which could be caused by a higher uncertainty in inferring R_b in the observation compared to the simulation (>1.5 kpc) for this age range or a physically larger strength caused by interactions with the SMC and the MW. Besides the increase in migration strength <5 Gyr, the strength also peaks around 0.5, 2, and 3 Gyr, close to SF enhancements.

For ages greater than 5 Gyr, the majority of stars in our sample are born in the inner disk (see Figure 7). As a result, they can predominantly migrate outward, producing the net outward shift visible in Figure 8. In contrast, for ages younger than 5 Gyr, stars are born more uniformly across the disk. Consequently, the median value of ($R - R_b$) remains close to zero, reflecting the absence of a preferred migration direction. The right panel of Figure 8 indicates that the migration strength is significantly enhanced near major episodes of SF. Interestingly, at ages of 0.5 and 2 Gyr, we do not observe a significant preference in stellar birth radii within the disk, despite the elevated migration strength at those epochs. These increases in migration strength can be caused by external perturbation of the SMC on the LMC during pericenter passages (e.g., A. C. Quillen et al. 2009; D. Hebrail et al. 2025).

3.3. The Chemodynamic History of the LMC

With R_b, we are able to recover the chemodynamic history of the LMC empirically. We do so by looking at the age–metallicity, age–[/M], and [Fe/H]–[/M] relations in mono-R_b and mono-age populations.

Figure 9 shows the age–metallicity (left) and age–[/M] (right) relations in mono-R_b and mono-age populations. Each colored line shows the median evolution of the abundances of stars in a 2 kpc R_b bin. The white segments show the times at which SF enhancements are observed. During the enhancements at 1, 3, and 5 Gyr, the overall metallicity goes down or stays constant at all radii, suggesting dilution from pristine gas. This also matches with the enhancement of SF during those times, as observed in Figure 7. Since the majority of SF 5 Gyr ago is concentrated in the inner disk, elements should be produced mostly in the central region. As a result, [/M] only increases for mono-R_b tracks $<$ 5 kpc, and [/M] decreases in the outer disk, where star formation efficiency (SFE) is low and no elements are produced. At 3 Gyr, the SF spreads across the entire disk, and thus [/M] increases for almost all mono-R_b tracks, thanks to the contribution of the Type II supernova (SN II) from these newly formed stars. At 1 Gyr, it is possible that the LMC did not accrete a significant amount of gas, given the minor decrease in [Fe/H]. The decrease of [/M] at all radii during that time suggests the SFE is not high. These tracks place strong constraints on the gas accretion and SFH at various locations and times.

Figure 10 shows the temporal evolution of [/M]-[Fe/H] for various radii. The biggest panel on the top right shows the mono-R_b tracks, similar to what is done in Figure 9. The smaller panels show the density and median abundances for stars in different R_b bins, increasing from the top left to the

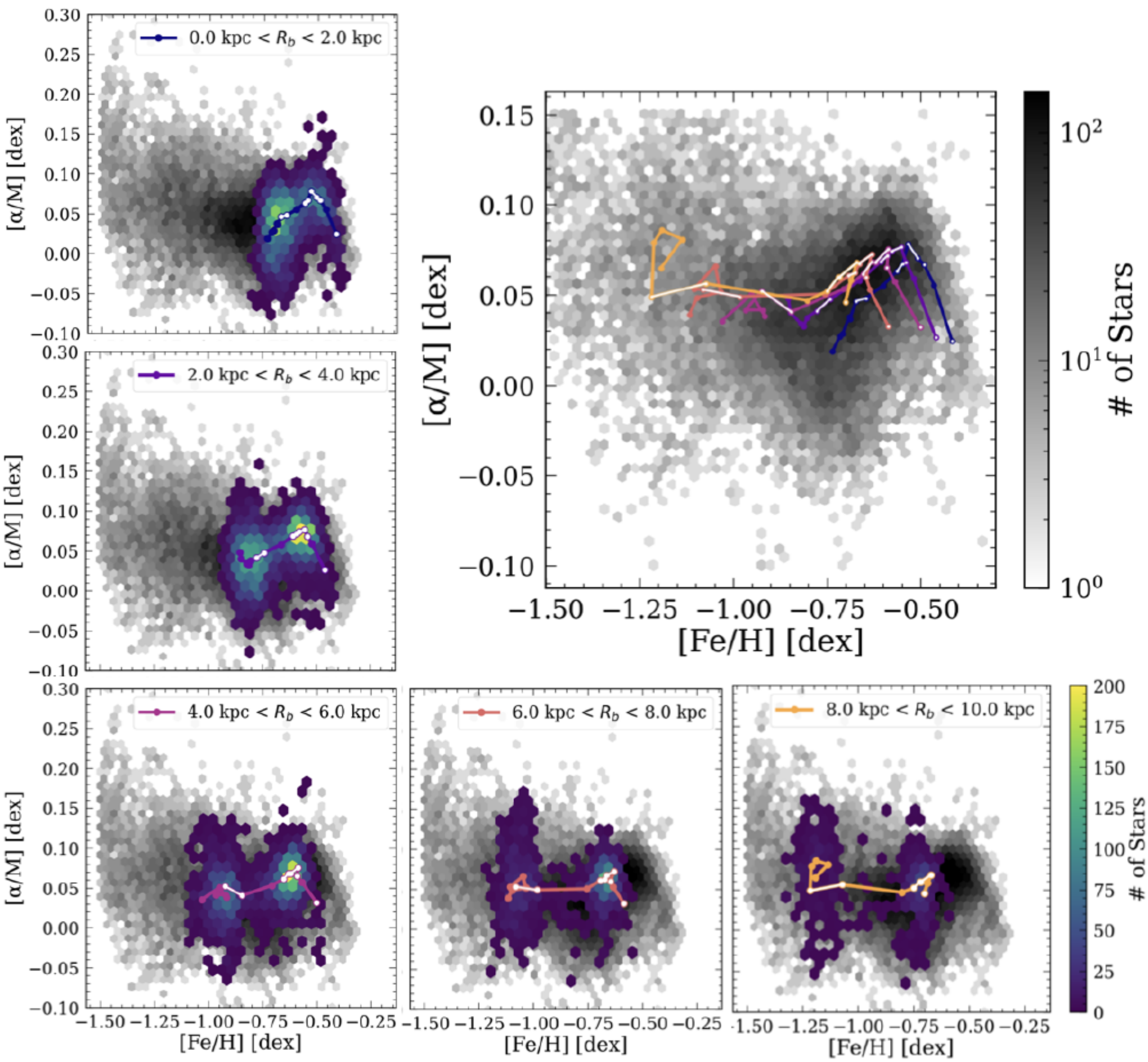

Figure 10. The largest panel on the top right shows the median mono-R_b tracks in [/M]-[Fe/H] space, similar to what is done in Figure 9. The smaller panels show the density and median abundances for stars in different R_b bins, increasing from the top left (inner galaxy) to the bottom right (outer galaxy). The white lines and points mark the SF enhancements taken from P. Massana et al. (2022).

bottom right. The white lines and points mark the SF enhancements. Similar to what was found in the MW in Y. L. Lu et al. (2024b), the SF enhancements naturally show up as overdensities in mono-R_b populations. The most -enriched stars are formed during the SF enhancements 3–2 Gyr ago, mostly between 2 and 4 kpc. This is also the time when most of the stars are formed during the SF enhancement at 3 Gyr.

4. Insight into the Lack of [/M]-[Fe/H] Bimodality of the LMC

The MW exhibits a distinct gap between the high- and low- disk (e.g., T. Bensby et al. 2014; D. L. Nidever et al. 2014; M. R. Hayden et al. 2015), and popular theories include the two-infall model (e.g., C. Chiappini et al. 1997; E. Spitoni et al. 2021), clumpy SF (e.g., A. J. Clarke et al. 2019; B. R. Garver et al. 2023), radial migration (e.g., S. Sharma et al. 2022), and quenching in SF (e.g., A. Beane et al. 2025). Compared to the MW, the LMC does not show such a signature, which raises questions on whether the bimodality is a common feature in disk galaxies (see also the analysis on M31 in D. L. Nidever et al. 2024).

What is interesting is that looking at LMC stars in the mono-R_b population in Figure 10, overdensities in [/M]-[Fe/H] show up during times of SF enhancements, similar to what is seen in the MW (Y. L. Lu et al. 2024b). We compare the most prominent steepening of the metallicity gradient in both galaxies—at 5 Gyr ago for the LMC and 8 Gyr ago for the MW—during which the MW developed its low- disk. Examining Figure 7 in Y. L. Lu et al. (2024b), we suggest that the distinct bimodality observed in the MW's [/M]–[Fe/H] plane, compared to the LMC, may be attributed to the extended SFH in the MW's outskirts. This extended SF began around 8 Gyr ago and directly produced the most metal-poor low- stars. In contrast, SF in the outskirts of the LMC appears to have been suppressed during its corresponding gradient-steepening episode at 5 Gyr, preventing the formation of a similarly extended low- sequence. Moreover, the centrally concentrated SF in the LMC at this time mitigated the typical decline in [/M] caused by delayed Type Ia supernova (SN Ia) enrichment. The simultaneous increase in -element production from SN II explosions associated with new SF counteracts the SN Ia effect, resulting in little net change in [/M] in the inner disk during the 5 Gyr event, preventing any bimodality from forming in the inner disk.

In summary, the lack of bimodality in the [/M]-[Fe/H] plane for the LMC could likely be caused by a combination of the changes in star-forming regions and enrichment history.

5. Limitations

The main caveat is whether we can robustly recover R_b for the LMC, given its recent interaction with the SMC. Tests on the NIHAO simulation suite (L. Wang et al. 2015) suggest this should be feasible. In Y. Lu et al. (2024a), we showed that an LMC-like galaxy—with an estimated dark matter halo mass of $18.8^{+3.5} - 4.0 \times 10^{10}\,M_{\odot}$ (N. Shipp et al. 2021) and a current "diskiness" of $\langle v_{\phi}/\sigma_{v}$ 2.8 (Figure B.5 in Gaia Collaboration et al. 2021b)—can be used to infer R_b using the method described in Y. L. Lu et al. (2024b). In that work, we successfully recovered R_b for a simulated LMC-mass galaxy (halo mass 1.64×10^{11}, $M_{\odot}$) that had undergone a merger roughly 1 Gyr ago, similar to the recent interaction between the MCs. Additionally, we assume stars are born on circular orbits around their birth radii, which could be incorrect for the LMC given its interaction with the SMC and the MW. This could contribute to an additional scatter to the inferred birth radii. Accounting for this effect would require detailed dynamical modeling of the LMC potential, which is beyond the scope of the present study. However, our analysis on the simulation (Section 2.3) suggests we should still be able to recover R_b within reasonable uncertainty for the LMC. Furthermore, the simulation analyzed in this study (B. Garver et al. 2026, in preparation), which reproduces the interaction history of the MCs, also indicates that we should be able to robustly recover R_b for the LMC and extract meaningful insights into its migration and SFH. That said, our ability to validate the method is limited to simulations, and unforeseen effects from the MCs' interaction could hinder its applicability. Future work could test the method on other simulation suites (e.g., Ó. Jiménez-Arranz et al. 2024). Additional assumptions, such as the metallicity gradient being negative and approximately linear during the early formation of the LMC's stellar disk, may also introduce uncertainties.

6. Conclusion and Future Work

In this paper, we tested a previous method described in Y. L. Lu et al. (2024b) to infer birth radii (R_b) for star particles in a hydrodynamical simulation intended to reproduce the interaction history of the MCs. We then applied this method to infer birth radii for the LMC stars. Combining R_b and age information, we are able to study the chemodynamic history of the LMC in the context of its interaction with the SMC. We found the following:

1. At 5 Gyr, SF is concentrated in the inner disk. By 3 Gyr, it becomes more widespread, extending from the center to the outer disk. At 1 Gyr, the SF remains broadly distributed but shows renewed concentration in the inner disk. These differences, if caused by the interactions between the MCs, could be due to different alignments of the disk spin orientations (e.g., J. Moreno et al. 2015). However, if the SF enhancements do not track the pericenter passages of the SMC to the LMC, and the inferred passages are correct in model 2 from G. Besla et al. (2012), the SMC and LMC disk spin orientations are likely aligned and have not changed, as the SFs are concentrated in the middle and outer disk for all three predicted pericenter passage times.
2. The migration strength for the LMC is found to be comparable but slightly higher than that of the MW, after scaling by their scale length, with significant increase <5 Gyr and near SF enhancements.
3. The LMC does not exhibit a clear [/M]–[Fe/H] bimodality like that observed in the MW, despite showing similar signatures of significant gas accretion events. This difference is likely due to the centrally concentrated nature of SF in the LMC during these episodes, in contrast to the more spatially extended SF that occurred in the outskirts of the MW.

These relations place strong constraints on the formation of the LMC and the interaction history between the MCs. Future work should explore different simulation suites to better understand how merger orbits and gas accretion events (e.g., galactic fountains) can affect the SF region in the merging galaxies and explore different assumptions, as in this work, we assume stars preferentially migrate outward as a population.

Acknowledgments

Y.L. wants to thank James Johnson for the helpful discussion. B.G. and D.L.N. acknowledge support by NSF grants AST 1908331 and 2408159. We thank V. Debattista for the help running the Gasoline simulations. We thank the anonymous referee for the constructive comments and helpful suggestions, which improved the clarity and quality of this manuscript. N.G.C. acknowledges support provided by the Heising-Simons Foundation grant # 2022-3927. This work has made use of data from the European Space Agency (ESA) mission Gaia,[8] processed by the Gaia Data Processing and Analysis Consortium (DPAC).[9] Funding for the DPAC has been provided by national institutions, in particular the institutions participating in the Gaia Multilateral Agreement. This research also made use of public auxiliary data provided by ESA/Gaia/DPAC/CU5 and prepared by Carine Babusiaux. This research has also made use of NASA's Astrophysics Data System.

Facilities: Gaia (Gaia Collaboration et al. 2016 2021a), Sloan (M. F. Skrutskie et al. 2006), Du Pont (J. C. Wilson et al. 2019).

Software: astropy (Astropy Collaboration et al. 2013; A. M. Price-Whelan et al. 2018; Astropy Collaboration et al. 2022), Matplotlib (J. D. Hunter 2007), NumPy (C. R. Harris et al. 2020), Pandas (W. McKinney et al. 2010), `ChatGPT` (OpenAI 2025).

[8] https://www.cosmos.esa.int/gaia
[9] https://www.cosmos.esa.int/web/gaia/dpac/consortium

ORCID iDs

Yuxi(Lucy) Lu https://orcid.org/0000-0003-4769-3273
Bethany Garver https://orcid.org/0000-0001-6013-9125
David L. Nidever https://orcid.org/0000-0002-1793-3689
Joshua T. Povick https://orcid.org/0000-0002-6553-7082
Nicolás Garavito-Camargo https://orcid.org/0000-0001-7107-1744
Maria-Rosa L. Cioni https://orcid.org/0000-0002-6797-696X
Danny Horta https://orcid.org/0000-0003-1856-2151

References

Abdurro'uf, Accetta, K., Aerts, C., et al. 2022, ApJS, 259, 35
Alves, D. R. 2004, ApJL, 601, L151
Astropy Collaboration, Price-Whelan, A. M., Lim, P. L., et al. 2022, ApJ, 935, 167
Astropy Collaboration, Robitaille, T. P., Tollerud, E. J., et al. 2013, A&A, 558, A33
Beane, A., Johnson, J. W., Semenov, V. A., et al. 2025, ApJ, 985, 221
Bensby, T., Feltzing, S., & Oey, M. S. 2014, A&A, 562, A71
Bernaldez, J. P., Minchev, I., Ratcliffe, B., et al. 2025, arXiv:2508.19340
Besla, G., Kallivayalil, N., Hernquist, L., et al. 2012, MNRAS, 421, 2109
Bland-Hawthorn, J., & Gerhard, O. 2016, ARA&A, 54, 529
Bressan, A., Marigo, P., Girardi, L., et al. 2012, MNRAS, 427, 127
Buck, T., Obreja, A., Ratcliffe, B., et al. 2023, MNRAS, 523, 1565
Chiappini, C., Matteucci, F., & Gratton, R. 1997, ApJ, 477, 765
Choi, Y., Nidever, D. L., Olsen, K., et al. 2018a, ApJ, 866, 90
Choi, Y., Nidever, D. L., Olsen, K., et al. 2018b, ApJ, 869, 125
Cioni, M. R. L. 2016, ASSP, 42, 49
Clarke, A. J., Debattista, V. P., Nidever, D. L., et al. 2019, MNRAS, 484, 3476
Cross, N. J. G., Collins, R. S., Mann, R. G., et al. 2012, A&A, 548, A119
Frankel, N., Andrae, R., Rix, H.-W., Povick, J., & Chandra, V. 2025, ApJ, 979, 136
Frankel, N., Sanders, J., Rix, H.-W., Ting, Y.-S., & Ness, M. 2019, ApJ, 884, 884
Frankel, N., Sanders, J., Ting, Y.-S., & Rix, H.-W. 2020, ApJ, 896, 15
Gaia Collaboration, Brown, A. G. A., Vallenari, A., et al. 2021a, A&A, 649, A1
Gaia Collaboration, Luri, X., Chemin, L., et al. 2021b, A&A, 649, A7
Gaia Collaboration, Prusti, T., de Bruijne, J., H., J., et al. 2016, A&A, 595, A1
Gallart, C., Meschin, I., Aparicio, A., Stetson, P. B., & Hidalgo, S. L. 2009, IAUS, 256, 281
Garver, B. R., Nidever, D. L., Debattista, V. P., Beraldo e Silva, L., & Khachaturyants, T. 2023, ApJ, 953, 128
Girardi, L., Bertelli, G., Bressan, A., et al. 2002, A&A, 391, 195
Harris, C. R., Millman, K. J., van der Walt, S. J., et al. 2020, Natur, 585, 357
Hayden, M. R., Bovy, J., Holtzman, J. A., et al. 2015, ApJ, 808, 132
Hebrail, D., Jiménez-Arranz, Ó., & Roca-F`abrega, S. 2025, A&A, 704, A90
Hunter, J. D. 2007, CSE, 9, 90
Jiménez-Arranz, Ó., Roca-F`abrega, S., Romero-Gómez, M., et al. 2024, A&A, 688, A51
Lian, J., Zasowski, G., Hasselquist, S., et al. 2022, MNRAS, 511, 5639
Loebman, S. R., Debattista, V. P., Nidever, D. L., et al. 2016, ApJL, 818, L6
Lu, Y., Buck, T., Minchev, I., & Ness, M. K. 2022a, MNRAS, 515, L34
Lu, Y., Buck, T., Nidever, D., et al. 2024a, MNRAS, 532, 411
Lu, Y. L., Minchev, I., Buck, T., et al. 2024b, MNRAS, 535, 392
Lu, Y. L., Ness, M. K., Buck, T., & Carr, C. 2022b, MNRAS, 512, 4697
Majewski, S. R., Schiavon, R. P., Frinchaboy, P. M., et al. 2017, AJ, 154, 94
Marigo, P., Girardi, L., Bressan, A., et al. 2017, ApJ, 835, 77
Massana, P., Ruiz-Lara, T., Noël, N. E. D., et al. 2022, MNRAS, 513, L40
Mazzi, A., Girardi, L., Zaggia, S., et al. 2021, MNRAS, 508, 245
McKinney, W., et al. 2010, in Proc. 9th Python in Science Conf., 445, 51
Minchev, I., Anders, F., Recio-Blanco, A., et al. 2018, MNRAS, 481, 1645
Minchev, I., Attard, K., Ratcliffe, B., et al. 2026, A&A, 706, A31
Minchev, I., Chiappini, C., & Martig, M. 2013, A&A, 558, A9
Minchev, I., & Famaey, B. 2010, ApJ, 722, 112
Moreno, J., Torrey, P., Ellison, S. L., et al. 2015, MNRAS, 448, 1107
Nidever, D. L., Bovy, J., Bird, J. C., et al. 2014, ApJ, 796, 38
Nidever, D. L., Gilbert, K., Tollerud, E., et al. 2024, IAUS, 377, 115
Nidever, D. L., Hasselquist, S., Hayes, C. R., et al. 2020, ApJ, 895, 88
Nidever, D. L., Holtzman, J. A., Allende Prieto, C., et al. 2015, AJ, 150, 173
Nidever, D. L., Olsen, K., Choi, Y., et al. 2021, AJ, 161, 74
Nidever, D. L., Olsen, K., Walker, A. R., et al. 2017, AJ, 154, 199
OpenAI 2025, ChatGPT (July 2025 version), https://chat.openai.com
Pardy, S. A., D'Onghia, E., & Fox, A. J. 2018, ApJ, 857, 101
Povick, J. T., Nidever, D. L., Majewski, S. R., et al. 2025, MNRAS, 544, 457
Povick, J. T., Nidever, D. L., Massana, P., et al. 2024, MNRAS, 533, 3685
Price-Whelan, A. M., Sipőcz, B. M., Günther, H. M., et al. 2018, AJ, 156, 123
Quillen, A. C., Minchev, I., Bland-Hawthorn, J., & Haywood, M. 2009, MNRAS, 397, 1599
Ratcliffe, B., Khoperskov, S., Lee, N., et al. 2026, A&A, 706, A103
Ratcliffe, B., Khoperskov, S., Minchev, I., et al. 2024, A&A, 690, A352
Ratcliffe, B., Minchev, I., Anders, F., et al. 2023, MNRAS, 525, 2208
Roškar, R., Debattista, V. P., Stinson, G. S., et al. 2008, ApJL, 675, L65
Rubele, S., Pastorelli, G., Girardi, L., et al. 2018, MNRAS, 478, 5017
Ruiz-Lara, T., Gallart, C., Monelli, M., et al. 2020, A&A, 639, L3
Sahlholdt, C. L., Feltzing, S., & Feuillet, D. K. 2022, MNRAS, 510, 4669
Salaris, M., Chieffi, A., & Straniero, O. 1993, ApJ, 414, 580
Saroon, S., Dias, B., Tsujimotto, T., et al. 2025, A&A, 701, A222
Sellwood, J. A., & Binney, J. J. 2002, MNRAS, 336, 785
Sharma, S., Hayden, M. R., Bland-Hawthorn, J., et al. 2022, MNRAS, 510, 734
Shipp, N., Erkal, D., Drlica-Wagner, A., et al. 2021, ApJ, 923, 149
Skrutskie, M. F., Cutri, R. M., Stiening, R., et al. 2006, AJ, 131, 1163
Spitoni, E., Verma, K., Silva Aguirre, V., et al. 2021, A&A, 647, A73
Torrey, P., Cox, T. J., Kewley, L., & Hernquist, L. 2012, ApJ, 746, 108
Vasiliev, E. 2024, MNRAS, 527, 437
Wadsley, J. W., Keller, B. W., & Quinn, T. R. 2017, MNRAS, 471, 2357
Wadsley, J. W., Stadel, J., & Quinn, T. 2004, NewA, 9, 137
Wang, L., Dutton, A. A., Stinson, G. S., et al. 2015, MNRAS, 454, 83
Wilson, J. C., Hearty, F. R., Skrutskie, M. F., et al. 2019, PASP, 131, 055001
Zhang, H., Belokurov, V., Evans, N. W., et al. 2025, ApJL, 983, L10